Case Studies in Thermal Engineering 61 (2024) 104874

Contents lists available at ScienceDirect

Case Studies in Thermal Engineering

journal homepage: www.elsevier.com/locate/csite

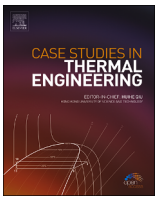

Numerical study and parametric analysis of thermo-hydraulic behavior in a flat loop heat pipe at system scale

Zikang Zhang [a, b], Haichuan Cui [a], Zhenyuan Ma [a], Yifan Zhang [a], Zhichun Liu [a], Wei Liu [a, *]

[a] School of Energy and Power Engineering, Huazhong University of Science and Technology, Wuhan, 430074, China
[b] Beijing Institute of Astronautics System Engineering, Beijing, 100076, China

ARTICLE INFO

Keywords:
Loop heat pipe
Two-phase flow simulation
Thermo-hydraulic behavior
Volume of fluid method
Parametric analysis

ABSTRACT

Using loop heat pipes (LHPs) for thermal management of aerospace and ground electronic devices has become an efficient and attractive method in recent years. A 3-D CFD numerical model was proposed for calculating the thermo-hydraulic behavior in a LHP with a square evaporator and the accuracy was verified by experimental results. The evaporation and condensation were addressed by volume of fluid method and a momentum source term derived from flow resistance analysis was incorporated into wick as the capillary force. The simulation results aligned with experimental trends, and errors of heating surface temperature and system thermal resistance were small. Due to structural constraint and gravity effect, two eddies were formed in compensation chamber, causing uneven distribution of temperature on heating surface. Parametric analysis indicated that higher porosity deteriorated the heat transfer from heating surface to wick and enlarged heating surface temperature and system thermal resistance. Higher wick and shell thermal conductivities ensured more heat conduction to the vapor-liquid interface and enhanced the evaporation intensity. However, the higher the thermal conductivity, the lower the improvement that could be obtained. Additionally, lower heat sink temperature and higher condenser heat transfer coefficient both intensified the LHP working performance by elevating the condensation efficiency.

1. Introduction

As the pillar industry of information technology, electronic devices have been widely used in modern tools such as mobile phones, computer servers, satellites, etc. According to Moore's law, miniaturization, integration, and efficiency are the critical development direction of the semiconductor chips in electronic devices, which further increases the possibility of thermal failure due to high heat accumulation. By combining two-phase cooling and passive transfer mechanism together, loop heat pipes (LHPs) display the merits of high efficiency, long distance, flexible arrangement, and strong stabilization [1], and meet the demands of thermal control systems in electronic devices. Thus, the LHPs have been used in broad scenarios including aerospace satellites [2,3], laptops and phones [4,5], data centers [6,7], electric vehicles [8,9], and power semiconductors [10], etc.

The main components of LHP include an evaporator, a condenser, and two transport lines. The capillary force is produced by a wick at the evaporator center, and the compensation chamber is separated from the vapor collector to maintain a proper vapor-liquid distribution. After entering the compensation chamber, the subcooled liquid absorbs a small amount of heat leaked from wick surface

* Corresponding author.
E-mail address: w_liu@hust.edu.cn (W. Liu).

https://doi.org/10.1016/j.csite.2024.104874
Received 2 November 2023; Received in revised form 15 July 2024; Accepted 20 July 2024
Available online 21 July 2024

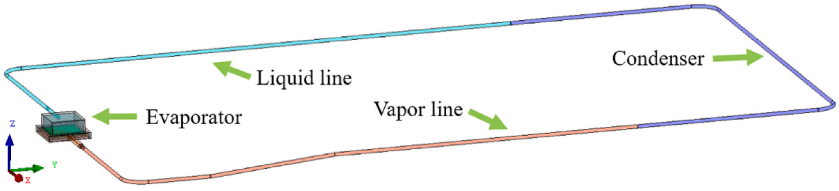

Fig. 1. The 3-D CFD model of the system.

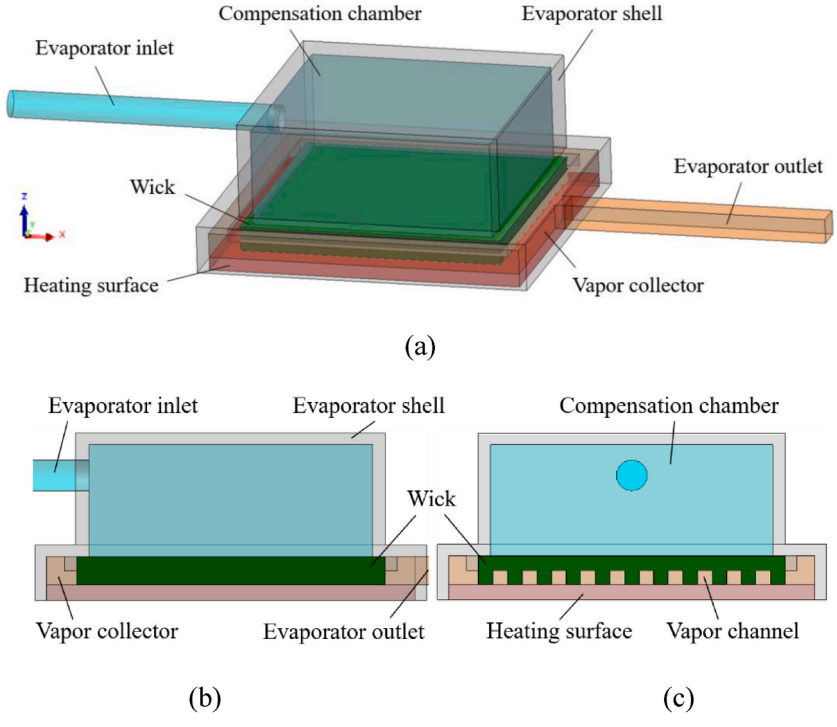

Fig. 2. The computation domain of the square plate evaporator. (a) The global structure. (b) The X-Z cross section. (c)The Y-Z cross section.

and evaporator shell before penetrating into the wick. Then, the liquid in wick is driven to the vapor-liquid menisci, absorbs the heat from the heating surface, and turns into vapor before entering the vapor channels and collector. The vapor flows through the vapor line and enters the condenser, releasing the heat to it and changing into subcooled liquid. Finally, the subcooled liquid returns from condenser to compensation chamber and a two-phase closed loop can be formed. Maydanik et al. [11] tested two ammonia LHPs with cylindrical and flat evaporators, which were two typical shapes of the evaporators in LHP systems. Comparative analysis indicated that LHP with a cylindrical evaporator produced stronger capillary force by a wider vapor-liquid interface and was less sensitive to internal pressure alternation than the flat one. LHP with a flat evaporator had a more isothermal contact surface and provided a more uniform thermal path than the cylindrical one, and was also lighter and more versatile since no saddle structure was required. Li et al. [12] used porous Si_3N_4 ceramics to fabricate the wicks and analyzed the effect of pore structures in a novel LHP. Wicks with bimodal pore structure exhibited stronger liquid uptake capacity than those with monomodal pore structure, and better capillary performance of the wick could be realized using a working fluid with lower viscosity, larger density, and higher surface tension. Baek et al. [13] achieved 63 % reduction in minimum start-up heat load by adding a vapor bypass line to regulate the vapor and liquid phases dispersed in compensation chamber and vapor channel, respectively. Ahmed et al. [14] proposed a new structure micro LHP with a low undesirable heat leak effect and provided a new methodology for working fluid selection. With an overall depth of 150 μm and a cross-section of 35 × 17 mm^2, the micro LHP using methanol as the working fluid achieved a temperature reduction of 28.6 °C at a heat load of 3.78 W. Tharayil et al. [15] used graphene-water nanofluid as the working fluid and tested a miniature LHP with a square flat evaporator. Results indicated that an optimum volume fraction of 0.006 % graphene nanosheets with distilled water was 21.6 % lower in minimum thermal resistance than that of pure distilled water. Liu et al. [16] proposed a LHP with a flow boiling chamber incorporated and visualized the vapor-liquid phase change process in compensation chamber. Both the capillary force in wick and the vapor through an injector drove the fluid circulation. The maximum heat flux reached 103.3 W/cm^2, indicating that this structure was a promising solution for high heat load conditions. Setyawan et al. [17] adopted a diaphragm pump to assisted the fluid circulation in a LHP. The dry-out in the evaporator was prevented and a significant reduction in heating surface temperature was observed.

Table 1
Structure parameters of the 3-D numerical model.

Component	Dimension	Value	Component	Dimension	Value
Evaporator shell	Length/Width	50.6/50.6 mm	Porous wick	Length/Width	39.76/39.76 mm
	Height	21.73 mm		Height	3.72 mm
	Material	SS304		Porosity	74.94 %
Compensation chamber	Length/Width	36.7/36.7 mm		Pore diameter	0.026 mm
	Height	14.51 mm		Material	Nickel
Vapor line	diameter	4 mm	Condenser	diameter	4 mm
	Length	784.5 mm		Length	950 mm
Liquid line	diameter	4 mm	Heating surface	Material	SS304
	Length	786 mm	Working fluid	Material	Ammonia

Table 2
Grid independence verification by three sets of grids.

Grid element number	Heating surface temperature			Evaporator outlet temperature		
	Simulation (K)	Experiment (K)	Error (%)	Simulation (K)	Experiment (K)	Error (%)
3547154	307.913	305.165	8.68 %	293.334	293.138	0.62 %
6875097	305.691	305.165	1.66 %	292.331	293.138	2.55 %
13956083	306.306	305.165	3.61 %	292.393	293.138	2.35 %

In recent years, numerous researches on LHP improvements are carried out experimentally due to the test results being more objective and intuitive. However, the complicated phase-change process limits the thermo-hydraulic behavior investigation of the loop from the experimental point of view. In addition, efforts involved in the experimental fabrications of the loop are huge and the results are rather unpredictable. Therefore, more numerical simulations and mechanism researches are required to reveal the thermo-hydraulic mechanisms so as to provide a guidance for further optimization in LHP performance.

Divided by the model categories, there are two types of LHP numerical simulation methods: one is to calculate the loop thermal response by mathematical models or thermal resistance networks, the other is to simulate the actual two-phase flow in components and even the whole loop by CFD analysis. Siedel et al. [18] developed a steady-state model combining the energy balance equations of the system with the 2D solutions of evaporator temperature field. Five parameters on the LHP operation were assessed and the model conformed with the experimental results. Belov et al. [19] presented a procedure for calculating the liquid and vapor resistances and heat flux balances to determine LHP steady-state performance, and the predictions were identical with the test results. Bai et al. [20] established a steady-state mathematical model based on gravity driven mode and capillary-gravity co-driven mode. These two modes could be distinguished by the transition heat load, which increased linearly with the positive elevation. Tharayil et al. [21] used thermal resistance network together with entropy generation analysis to model a miniature LHP with graphene-water nanofluid and found that the nanofluid reduced the entropy generation and increased the second law efficiency. Qu et al. [22] calculated the heat leak effect in a global model of cryogenic LHP with the help of one-dimensional temperature distributions in the evaporator and two new evaporating temperature curves were found at moderate and high filling pressures. Meinicke et al. [23] captured the LHP transient thermal characteristics by calculating and updating the mass flow rate and phase distribution separately in a mathematical model. Two different LHPs performed high coincidence between the predictions and the experimental results. Liu et al. [24] proposed a big-data-driven prediction model for the LHP heat transfer limit based on the neural network and grey correlation method. The optimal simulation effect was achieved when the number of neurons was 100 and the average relative error was 0.32 %. Bernagozzi et al. [25] predicted the LHP transient behavior by a 1-D lumped parameter model at various boundary and initial conditions, through which quick feasibility studies with high accuracy could be achieved.

For further detailed calculation on the thermo-hydraulic behavior of working fluid, CFD calculation method could be occupy to determine the two-phase and heat flux distributions inside each component of the LHP. Li et al. [26] developed three-dimensional governing equations and set up a practical 3-D numerical model with a fully saturated wick structure in a square plate evaporator. Fukushima et al. [27] took the peculiarities of evaporator structure and one side heat load supply into account in a 3-D micro-LHP model, thus achieving a good prediction of the system temperature distributions. With the EFDLab software implemented, Chernysheva et al. [28] constructed a 3-D flat evaporator model and calculated flow field and temperature distribution in the compensation chamber. They observed that the internal heat transfer intensity was depended on the evaporator orientation. Zhang et al. [29] calculated the unit cell of wick and vapor groove in a complete 3-D model and revealed that the heat transfer coefficient inside the wick was greater than that inside the solid wall at wick saturated status. Li et al. [30] built a pore scale model by an advanced phase-change Lattice Boltzmann Method in evaporator and observed five patterns appearing at vapor-liquid interface under different heat flux conditions. Mottet et al. [31] built wick structures with a two-scale cubic network of pores and throats. The vapor and liquid phase distributions could be well reconstructed and the bidispersed wick created preferential vapor paths as well as a wider two-phase zone than the monodispersed wick. Zhang et al. [32] cooperated CFD numerical simulation with the VOF multiphase flow method to assess the heat leak effect in a flat evaporator with carbon fiber wick. Better thermal insulation material (yttria-stabilized zirconia) could largely enhance the operation stability by raising the liquid volume fraction in the compensation chamber. Pozhilov et al. [33] employed

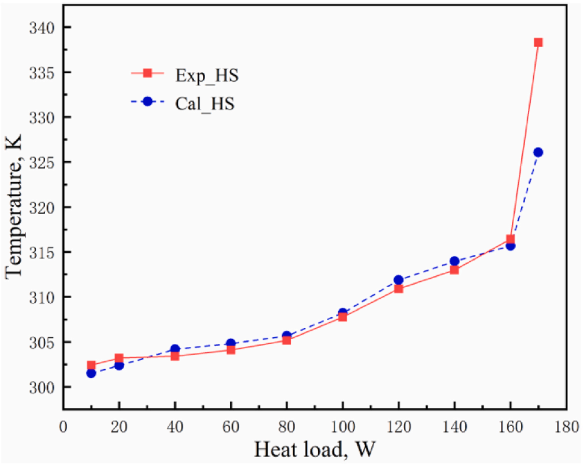

Fig. 3. Comparison of numerical and experimental results against various heat loads at heat sink temperature of 0 °C. (a) Heating surface temperature. (b) LHP thermal resistance.

Reynolds-averaged Navier-Stokes equations, Darcy's law, and energy equations to simulate the conjugate heat and flow transfer process, and revealed the behavior of the non-uniform heat flux density in a 3-D cylindrical evaporator model.

In conclusion, the simulation methods above either parametrically solved the thermal transfer process of the LHP from the perspective of mathematical solutions, or specifically analyzed the thermo-hydraulic process by determining the two phase flow field on the unit cell of wick or partial component of the loop. However, rare works have focused on conjunct calculation of thermal transfer process and two-phase flow field at the entire LHP scale, let alone further parametric analysis of the loop operating performance. In this paper, a comprehensive 3-D CFD numerical model was proposed for calculating thermo-hydraulic behavior and phase change process at the whole system scale. The volume of fluid method was adopted to construct the vapor-liquid interface and a momentum source term determined by the flow resistance analysis was added to wick domain to imitate the capillary force. Compared with the experiment results in previous study, the simulation results showed good accuracy in terms of temperature and thermal resistance variation trends. In addition, the effects of design parameters including porosities, wick and shell thermal conductivities, condenser temperatures and coefficients on heat transfer and phase distribution were specifically analyzed. This would help to enhance the LHP operating performance by optimizing different design parameters according to various structural selections and application scenarios in the future research work.

2. Numerical model

2.1. Multiphase flow model description

The volume of fluid method of Lee model [34] is a effective way to simulate the flow and volume fraction variation of two or more immiscible fluids, making it suitable for multiphase flow calculation with complex phase change and heat transfer mechanisms. The

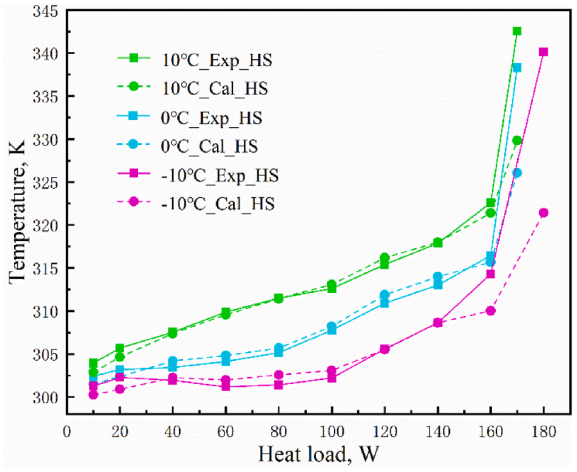

(a)

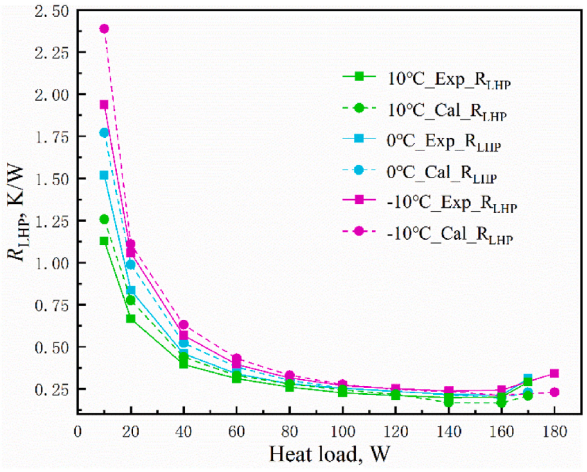

(b)

Fig. 4. Comparison of numerical and experimental results against various heat sink temperatures. (a) Heating surface temperature. (b) LHP thermal resistance.

governing equations of continuity, momentum, and energy are established for the heat transfer and two-phase flow processes. The assumptions including that the thermophysical properties of fluid remain constant, the fluid is incompressible, and the continuous flow hypothesis is satisfied, are needed to be made.

According to the mass conservation law, the sum of liquid and vapor volume fractions is equal to 1 [35],

$$\alpha_l + \alpha_v = 1 \tag{1}$$

The continuity equations of two volume fractions can be expressed as follows [34],

$$\frac{\partial \alpha_l \rho_l}{\partial t} + \nabla \cdot \left(\vec{u}\alpha_l \rho_l\right) = S_{m,l} \tag{2}$$

$$\frac{\partial \alpha_v \rho_v}{\partial t} + \nabla \cdot \left(\vec{u}\alpha_v \rho_v\right) = S_{m,v} \tag{3}$$

where $S_{m,v}$ and $S_{m,l}$ represent the vapor and liquid mass transfer rates (source terms), respectively. By comparing the saturation temperature of fluid with the local temperature of cell, the two fluid mass transfer rates can be calculated as [34],

$$S_{m,v} = coeff \cdot \alpha_l \rho_l \frac{|T_l - T_{sat}|}{T_{sat}} \quad T_l \geq T_{sat}, \text{(evaporation)} \tag{4}$$

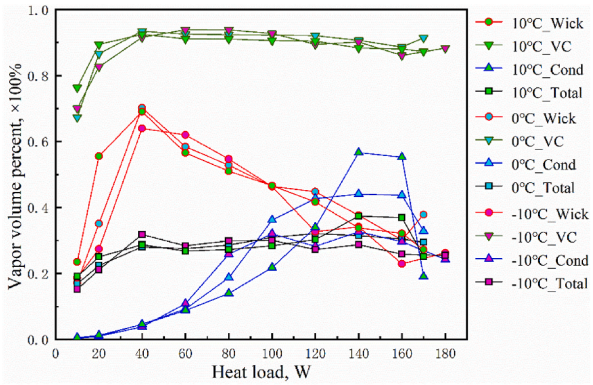

Fig. 5. Vapor volume percent variation of different fluid domains in relation to heat load and heat sink temperature.

$$S_{m,l} = coeff \cdot \alpha_v \rho_v \frac{|T_{sat} - T_v|}{T_{sat}} \quad T_v \le T_{sat}, \text{(condensation)} \tag{5}$$

where *coeff* is the mass transfer coefficient derived from the Hertz-Knudsen equation [36,37] and can be fine defined as,

$$coeff = \frac{6}{d_b}\sqrt{\frac{M}{2\pi R_g T_{sat}}} h_{fg} \left(\frac{\alpha_v \rho_v}{\rho_l - \rho_v}\right) \tag{6}$$

where d_b is the bubbled diameter, R_g is the universal gas constant, M is the relative molecule mass, and h_{fg} is the latent heat of working fluid.

The momentum equation considers the effects of friction, gravitation, and surface tension, and has the following form [38,39],

$$\frac{\partial \rho \vec{u}}{\partial t} + \nabla \cdot \left(\rho \vec{u}\vec{u}\right) = -\nabla p + \nabla \cdot \left[\mu\left(\nabla \vec{u} + \nabla \vec{u}^T\right)\right] + \rho \vec{g} + F_{vol} \tag{7}$$

where ρ and μ are the volume-averaged density and viscosity of all phases, F_{vol} is the surface tension (source term) and is proportional to the volume-averaged density in the cell according to the continuum surface force model [40],

$$F_{vol} = \sigma \frac{\alpha_l \rho_l \kappa_v \nabla \alpha_v + \alpha_v \rho_v \kappa_l \nabla \alpha_l}{0.5\left(\rho_l + \rho_l\right)} \tag{8}$$

where σ is the surface tension coefficient, κ is the interphase curvature and can be defined by the divergence of the unit normal vector.

The energy equation for the fluid regions is shared among two phases and has the following form [38,39],

$$\frac{\partial}{\partial t}(\rho E) + \nabla \cdot \left[\vec{u}(\rho E + p)\right] = \nabla \cdot [k \nabla T] + S_q \tag{9}$$

where E and T are treated as mass-averaged energy and temperature, k is the volume-averaged thermal conductivity of all phases, S_q is the heat source (source term) contributed by the fluid evaporation and condensation and it observes [35],

$$S_q = -h_{fg} S_{m,l} = h_{fg} S_{m,v} \tag{10}$$

Four source terms mentioned above (fluid mass transfer rates, surface tension, and heat source) are added to the governing equations by using User-define functions in the computation model.

The energy equation for the solid origins follows heat conduction law and can be written as [35],

$$\frac{\partial}{\partial t}(\rho h) = \nabla \cdot \left[k_s \nabla T\right] \tag{11}$$

where k_s and h are the thermal conductivity and sensible enthalpy of the solid material, respectively.

The porous medium option in the computation model is used to simulate the pressure drop inside the porous wick. Specifically, viscous and inertial loss terms constitute the momentum source term [38],

$$S_{M,i} = -\left(C_1 \mu u_i + C_2 \frac{1}{2} \rho |u_i| u_i\right) \tag{12}$$

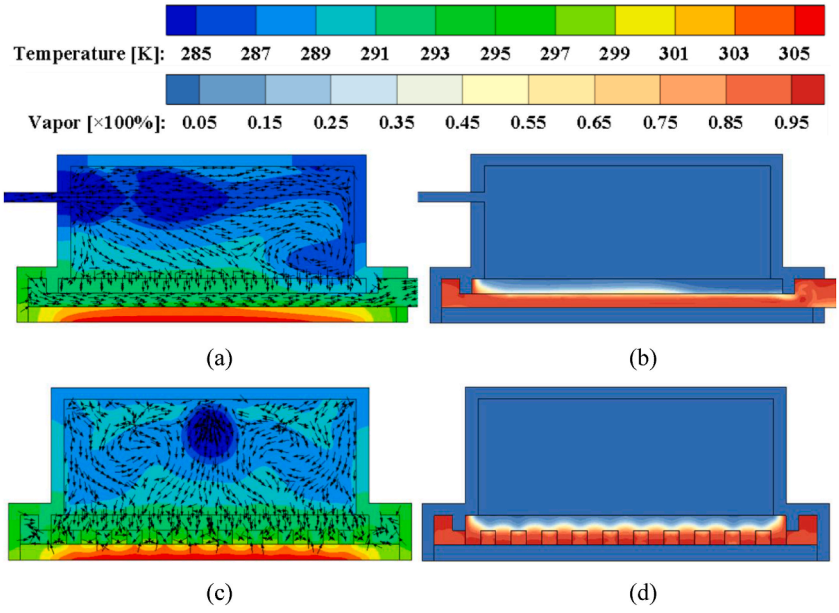

Fig. 6. Distributions of temperature, stream line, and vapor-liquid interface at heat sink temperature of 0 °C and heat load of 80 W. (a)(b) Vapor channel sections in X-direction. (c)(d) Evaporator central sections in Y-direction.

where $S_{M,i}$ represents the i-th phase source term that needed to be added to the flow equations, $|u_i|$ is the magnitude of the i-th phase velocity, C_1 and C_2 are the viscous and inertial resistance factors. By treating the wick as monoporous medium for simplification, the viscous and inertial resistance factors can be determined by Ergun equation [41],

$$\frac{1}{C_1} = \frac{{d_p}^2}{150}\frac{\phi^3}{(1-\phi)^2} \tag{13}$$

$$C_2 = \frac{3.5}{d_p}\frac{1-\phi}{\phi^2} \tag{14}$$

where ϕ is the wick porosity, d_p is the average pore diameter deduced from the actual pore structure.

Considering the wick domain as a stable thermal equilibrium state, the continuity, momentum, and energy equations of the wick domain can be derived with porosity and relevant source terms taken into account [34,38,39],

$$\phi\frac{\partial \alpha_l \rho_l}{\partial t} + \nabla\cdot\left(\vec{u}\alpha_l\rho_l\right) = S_{m,l} \tag{15}$$

$$\phi\frac{\partial \alpha_v \rho_v}{\partial t} + \nabla\cdot\left(\vec{u}\alpha_v\rho_v\right) = S_{m,v} \tag{16}$$

$$\frac{1}{\phi}\frac{\partial \rho\vec{u}}{\partial t} + \frac{1}{\phi^2}\nabla\cdot\left(\rho\vec{u}\vec{u}\right) = -\nabla p + \frac{1}{\phi}\nabla\cdot\left[\mu\left(\nabla\vec{u} + \nabla\vec{u}^T\right)\right] + \rho\vec{g} + F_{vol} + S_{M,i} + S_{cap} \tag{17}$$

$$\phi\frac{\partial}{\partial t}(\rho E) + \nabla\cdot\left[\vec{u}(\rho E + p)\right] = \phi\nabla\cdot[k\nabla T] + S_q \tag{18}$$

where u of the wick domain is the superficial velocity of fluid, S_{cap} is a momentum source term added on the wick domain to incorporate the effect of capillary force, which is derived in the following section.

2.2. LHP model geometry

As presented in Fig. 1, the computation domains of the LHP system include an evaporator, a condenser, vapor and liquid line. Fig. 2 illustrates that the evaporator is separated into three fluid domains: compensation chamber, porous wick, and vapor collector. A momentum source term incorporated on the wick domain acts as capillary force to maintain the working fluid circulation. Heat added on the heating surface is conducted through wick and evaporator shell, and is adsorbed by the latent heat of liquid vaporization in wick and sensible heat of subcooled fluid in compensation chamber, respectively. The condenser, vapor and liquid lines are simplified as thin, long tubes with temperatures and heat transfer coefficients as boundary conditions. The local mesh quality at the evaporator outlet is improved by modifying the evaporator outlet into a rectangular structure while maintaining the same hydraulic diameter as the other tubes, and also a small transition section is designed to connect the rectangular evaporator outlet and cylindrical vapor line.

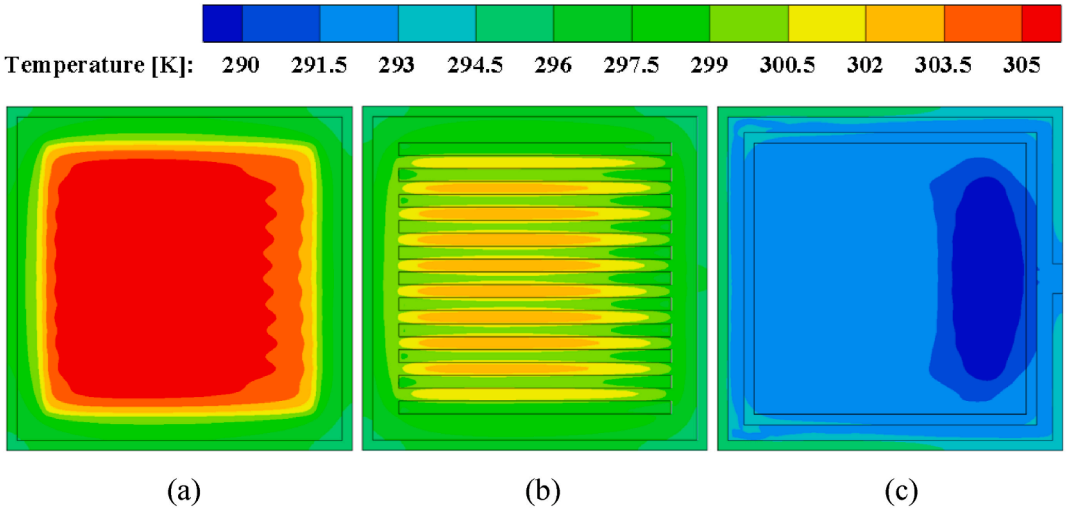

Fig. 7. Temperature distributions of three evaporator sections in different Z-directions at heat sink temperature of 0 ˚C and heat load of 80W. (a) Heating surface. (b) Contact surface between heating surface and rib. (c) Wick surface in compensation chamber.

Moreover, in order to verify the computation model accuracy by experiment results, the structure parameters illustrated in Table 1 are the same as those of the previous experimental investigation [42].

2.3. Flow resistance analysis

The 3-D numerical model in this paper is a closed loop operating passively. The capillary pressure generated by porous structure maintains the stable circulation of the fluid inside. According to Young-Laplace equation [43], the maximum capillary pressure can be calculated as,

$$\Delta P_{cap,max} = \frac{4\sigma \cos \theta}{d_p} \tag{19}$$

where θ is the contact angle between fluid and solid. However, the utilization degree of the porous structure is affected by different working conditions. The capillary pressure may not reach the theoretical maximum value especially at low and medium heat load conditions. From the perceptive of pressure balance, the stable operation of practical LHP system indicates that a quasi-steady condition will be established inside. For this reason, the actual capillary pressure is the same as the sum of flow resistances generated by LHP components,

$$\Delta P_{cap} = \Delta P_{tot} = \Delta P_{vl} + \Delta P_{ll} + \Delta P_{cond} + \Delta P_{cc} + \Delta P_{vch} + \Delta P_{vco} + \Delta P_{w} + \Delta P_{g} \tag{20}$$

where the terms on equation right side are the pressure losses of different components, specifically speaking, including vapor line (ΔP_{vl}), liquid line (ΔP_{ll}), condenser (ΔP_{cond}), compensation chamber (ΔP_{cc}), vapor channels (ΔP_{vch}), vapor collector (ΔP_{vco}), wick (ΔP_{w}), and gravity (ΔP_{g}). When the loop works at horizontal orientation, no altitude intercept exists between the evaporator and condenser, thus ΔP_{g} can be ignored consequently.

In addition to the wick and two-phase section of condenser, the pressure losses in other parts can be divided into viscous and local resistances. The Reynolds number for each flow zone is expressed as,

$$Re = \frac{4m_f}{\pi d_t \mu} \tag{21}$$

where d_t is the average hydraulic diameter associated with the structure parameter, m_f is the fluid mass flow rate. u is the fluid velocity and satisfies,

$$u = \frac{4m_f}{\pi \rho {d_t}^2} \tag{22}$$

The viscous pressure loss is calculated by Darcy-Weisbach equation [44],

$$\Delta P_{vis} = \xi \frac{\rho u^2 l}{2 d_t} \tag{23}$$

where l is the flow line length, ξ is the friction factor and can be calculated at different Re number,

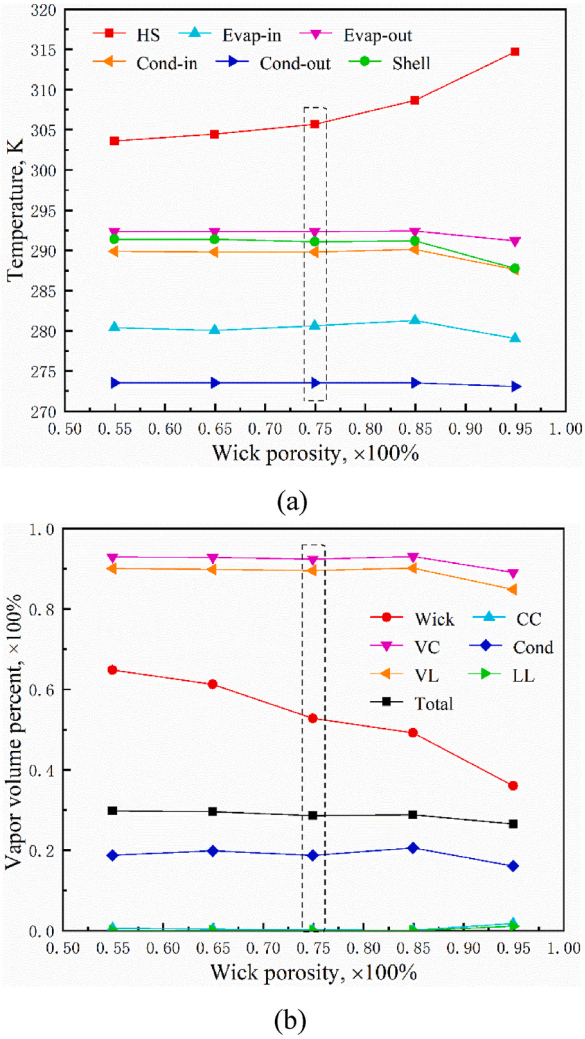

Fig. 8. Effect of different wick porosities on LHP components. (a) Temperature trend. (b) Vapor volume percent trend.

$$\xi = \frac{64}{Re} \quad Re \le 2300, \text{(laminar flow)} \tag{24}$$

$$\xi = \frac{0.3164}{Re^{0.25}} \quad Re \ge 5000, \text{(fully developed turbulent flow)} \tag{25}$$

$$\xi = \xi_{2300} + \frac{\xi_{5000} - \xi_{2300}}{5000 - 2300}(Re - 2300) \quad 2300 \le Re \le 5000, \text{(transition flow)} \tag{26}$$

where ξ_{2300} and ξ_{5000} are the friction factors at Re = 2300 and Re = 5000, respectively.

The local pressure loss can be calculated by local resistance coefficient,

$$\Delta P_{loc} = \zeta \frac{\rho u^2}{2} \tag{27}$$

where ζ is the local resistance coefficient, and it is a constant value related to the channel structure types, such as tube bend and joint shape.

The pressure loss ΔP_w in wick is described by Darcy's law [43],

$$\Delta P_w = \frac{\mu_l m_f L_w}{\rho_l K A_w} \tag{28}$$

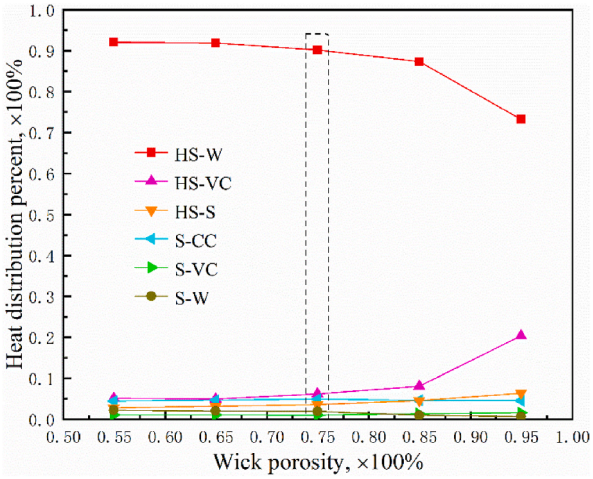

Fig. 9. Heat distribution of evaporator with different wick porosities.

where L_w is the capillary structure thickness, A_w is the wick surface area, K is the wick permeability deduced by Carman-Konzeny formula [43],

$$K = \frac{{d_p}^2 \phi^3}{180(1-\phi)^2} \tag{29}$$

The pressure loss of two-phase flow in condenser is added by three parts: frictional, acceleratory, and gravitational pressure drops [45,46],

$$\left(\frac{dP}{dL}\right)_f = -0.09\frac{{m_f}^2}{\rho_v g d_t}\left(\frac{m_f d_t}{\mu_v}\right)^{-0.2}\left[\begin{array}{l} x^{1.8} + 5.7\left(\frac{\mu_l}{\mu_v}\right)^{0.0523}(1-x)^{0.470}x^{1.33}\left(\frac{\rho_l}{\rho_v}\right)^{0.261} \\ +8.11\left(\frac{\mu_l}{\mu_v}\right)^{0.105}(1-x)^{0.94}x^{0.86}\left(\frac{\rho_l}{\rho_v}\right)^{0.522} \end{array}\right] \tag{30}$$

$$\left(\frac{dP}{dL}\right)_a = -\frac{{m_f}^2}{\rho_v g}\left(\frac{dx}{dL}\right)\left[2x + (1-2x)\left(\frac{\rho_v}{\rho_l}\right)^{1/3} + (1-2x)\left(\frac{\rho_v}{\rho_l}\right)^{2/3} - 2(1-x)\left(\frac{\rho_v}{\rho_l}\right)\right] \tag{31}$$

$$\left(\frac{dP}{dL}\right)_g = -g\ \sin\ \theta \cdot \left[x\rho_v + (1-x)\rho_l\right] \tag{32}$$

where the subscripts f, a, and g represent the frictional, acceleratory, and gravitational pressure drops respectively, x is the dryness degree of the fluid, and L is the length of two-phase segment. To simplify the pressure loss calculation of two-phase flow, the dryness degree is divided into ten sections with each section varying by $\Delta x = 0.1$. Hence, the length for each section can be expressed as,

$$L_{c,m} = \frac{m_f h_{fg} \Delta x}{4 h_z \Delta T} \tag{33}$$

where ΔT is the temperature difference between fluid and condenser tube wall, h_z is the local heat transfer coefficient determined by Ref. [46],

$$h_z = \frac{Nu k_l}{d_t} \tag{34}$$

where Nu is the Nusselt number relating to the local heat transfer coefficient and satisfies [46],

$$\frac{Nu \cdot F_2}{Pr_l \cdot Re_l} = F\left(X_{tt}\right) \quad 0.1 < F\left(X_{tt}\right) < 1 \tag{35}$$

$$\frac{Nu \cdot F_2}{Pr_l \cdot Re_l^{0.9}} = F\left(X_{tt}\right)^{1.15} \quad 1 < F\left(X_{tt}\right) < 20 \tag{36}$$

$$F\left(X_{tt}\right) = 0.15\left[X_{tt}^{-1} + 2.85 X_{tt}^{-0.476}\right] \tag{37}$$

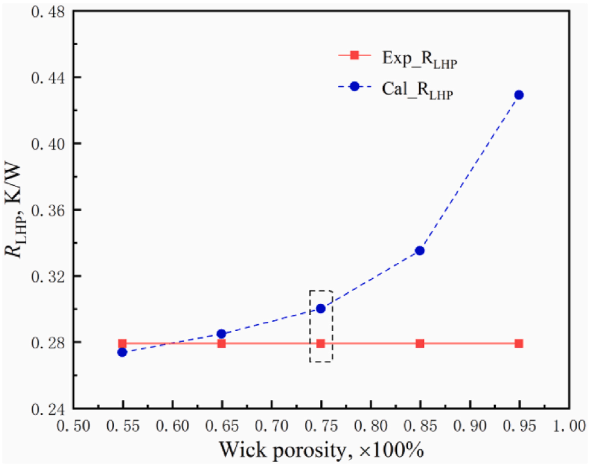

Fig. 10. The LHP thermal resistance with different wick porosities.

$$X_{tt} = \left(\frac{\mu_l}{\mu_v}\right)^{0.1} \left(\frac{1-x}{x}\right)^{0.9} \left(\frac{\rho_v}{\rho_l}\right)^{0.5} \tag{38}$$

where Re_l has the form [46],

$$Re_l = \frac{(1-x)\, m_f d_t}{\mu_l} \tag{39}$$

The F_2 can be determined by Ref. [46],

$$F_2 = 0.707 Pr Re_l^{0.5} \quad Re_l < 50 \tag{40}$$

$$F_2 = 5Pr_l + 5\ \ln\left(1 + Pr_l\left(0.09636 Re_l^{0.585} - 1\right)\right) \quad 50 \le Re_l < 1125 \tag{41}$$

$$F_2 = 5Pr_l + 5\ \ln\left(1 + 5Pr_l + 2.5\ \ln\left(0.0031 Re_l^{0.812}\right)\right) \quad Re_l \ge 1125 \tag{42}$$

where Pr is the Prandtl number related to the fluid physical parameters. According to Eqs. (28)–(37), the length of each two-phase segment $L_{c,m}$ corresponding to dryness alteration Δx can be numerically determined. To sum up these ten sections, the total length of two phase zone and pressure loss in condenser can be solved eventually.

As indicated from the above flow resistance analysis, functions between the mass flow rate m_f and the total flow resistance ΔP_{tot} can be set up, and for the circumstance of the LHP stable operation, Eq. (15) is always satisfied. Consequently, the actual capillary pressure ΔP_{cap} can be accurately calculated by reason of the mass flow rate m_f. According to the previous research [42], the working fluid in liquid line is affected by the ambient heat leakage and shows a significant temperature rise while reaching the evaporator inlet. The heat leakage between the ambient and liquid line can be calculated by a steady state heat conduction model of the cylinder wall, and it is also related to the latent heat, temperature rise, and mass flow rate of working fluid inside the tube. Hence, by adopting the experimental data, the mass flow rate m_f can be further deduced through the heat leakage effect of liquid line [42]. Finally, the capillary action of wick can be introduced into the CFD model by adding a momentum source term S_{cap} calculated from the actual capillary pressure ΔP_{cap} to the momentum equation of wick domain,

$$S_{cap} = \frac{\Delta P_{cap}}{L_w} \tag{43}$$

2.4. Boundary conditions

The boundary conditions of the model are determined according to the experimental results in pervious study [42]. The Archimedes method is adopted to derive the wick porosity, and the viscous model of fluid flow in wick is set as a laminar flow for the flow velocity inside is low. The thermophysical parameters of wick contain specific heat capacity, density, and effective thermal conductivity, and are averagely weighted and calculated by considering the porosity effect. The 3-D model has no inlet or outlet, which means that a momentum source term solved by the above flow resistance analysis is required to simulate the effect of capillary pressure and maintain the fluid circulation. The NIST software is used to deduce the thermophysical parameters of the vapor and fluid from vapor-liquid interface saturation temperature and evaporator inlet temperature. The vapor-liquid saturation temperature is chosen as the average of two temperatures at evaporator outlet and compensation chamber on account of the middle position of wick between these two places. The contact angle between fluid and solid is set at 50° on account of the good hydrophilicity and wettability

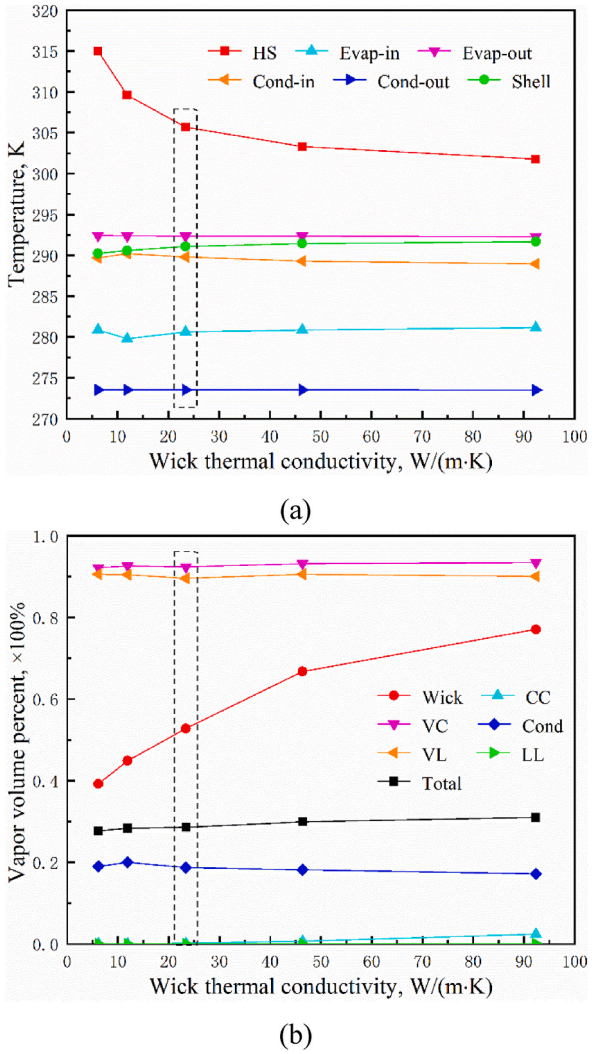

Fig. 11. Effect of different wick thermal conductivities on LHP components. (a) Temperature trend. (b) Vapor volume percent trend.

of the wick. Heat flux applied to the area of 40 × 40 mm^2 on the center of heating surface has the same value as that in the experiment. The wall boundary conditions of condenser, evaporator shell, liquid line, and vapor line, are composed of wall temperatures and heat transfer coefficients, and can be calculated separately according to the experimental results at each position. Additionally, interfaces between solid and fluid domains are set as coupled wall option, and between fluid domains are set as matching option.

2.5. Solution methods and mesh sensitivity

The numerical calculation of the 3-D model is carried out by Fluent 2019 R3 software. The implicit formulation VOF method with steady solution and pressure-based solver is adopted to solve the two-phase thermo-hydraulic process. Liquid is the primary phase and vapor is the secondary phase. The SST k-w format is selected for the turbulent model and the pressure-velocity coupling algorithm is the Coupled method. The discretization scheme is set as PRESTO for pressure, first-order upwind for turbulent kinetic energy and specific dissipation rate, compressive for volume fraction, QUICK for energy and momentum. The vapor-liquid interface is reconstructed by Piecewise Linear Interface Calculation method. The calculation is considered to be convergent when the vapor volume percent stabilizes and the residuals reach 10^{-3} and 10^{-6} for turbulence dissipation term and energy equation.

In order to speed up the calculation by improving the mesh quality, ICEM CFD 2019 R3 software is employed for mesh modeling. The whole loop first separates into several parts with multiple blocks, and each part is divided into full-hexahedral grid by the structured meshing method. Besides, Ogrid method is used for cylindrical structures in the model such as the liquid, vapor, and condenser lines. By adjusting the maximum grid size, three sets of grids are used for independence verification and the grid numbers are 3547154, 6875097, and 13956083, respectively. Table 2 depicts the comparison of simulation and experiment results under the same working condition (heat load of 120 W and heat sink temperature of 0 °C). The relative errors of evaporator outlet temperature remain below 3 % for the three sets of grids, and the relative error of heating surface temperature is below 2 % at the grid number of 6875097. In addition, as the grid number increases further, the simulation results of heating surface and evaporator outlet tempera-

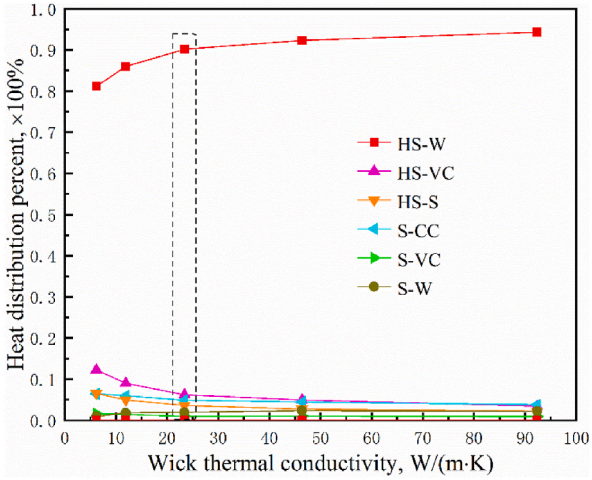

Fig. 12. Heat distribution of evaporator with different wick thermal conductivities.

tures are gradually stabilized. Therefore, in order to accelerate the computation, the grid number of 6875097 is chosen for the subsequent calculation.

3. Experimental validation

3.1. Comparison at various heat loads

By comparing with the experimental results, the model accuracy can be verified under various heat sink temperatures and heat loads. The error of heating surface temperature is defined as,

$$\varepsilon_{HS} = \frac{\left|T_{cal\_HS} - T_{exp\_evap\_in}\right|}{\left|T_{exp\_HS} - T_{exp\_evap\_in}\right|} \tag{44}$$

where T_{exp_HS} and T_{cal_HS} are the heating surface temperatures of the experimental and numerical results, $T_{exp\_evap\_in}$ is the evaporator inlet temperature of the experimental results. Acting as a reflection of the thermal transfer performance of the whole system, the LHP thermal resistances of the experimental and numerical results can be expressed by,

$$R_{exp\_LHP} = \frac{T_{exp\_HS} - T_{exp\_cond}}{Q} \tag{45}$$

$$R_{cal\_LHP} = \frac{T_{cal\_HS} - T_{cal\_cond}}{Q} \tag{46}$$

where Q is the heat load at heating surface, T_{exp_cond} and T_{cal_cond} are the condenser temperatures of the experimental and numerical results. The error of LHP thermal resistance is calculated by,

$$\varepsilon_R = \frac{\left|R_{cal\_LHP} - R_{exp\_LHP}\right|}{R_{exp\_LHP}} \tag{47}$$

Fig. 3 presents the comparison of numerical and experimental results on heating surface temperature and LHP thermal resistance against various heat loads at heat sink temperature of 0 °C. The heat load varied from 10 W to 170 W with an interval of 20 W. Apparently, an agreement was found at a wide range of heat load between numerical and experimental results. The numerical results indicated that the variation trends of heating surface temperature and LHP thermal resistance closely matched those of the experimental results. As the heat load reached the maximum, a serious dry-out state occurred in wick and vapor began to seep through the wick and even entered the compensation chamber. The vapor leakage in this process was too complex that the model was incapable of evaluating it mathematically. In addition to the extreme working conditions such as the maximum and minimum heat loads, the maximum errors of heating surface temperature and LHP thermal resistance were lower than 5.2 % and 13.5 %, respectively, which indicated that the 3-D computation model was an efficient and high accurate method for calculating the thermo-hydraulic behavior in actual LHP systems.

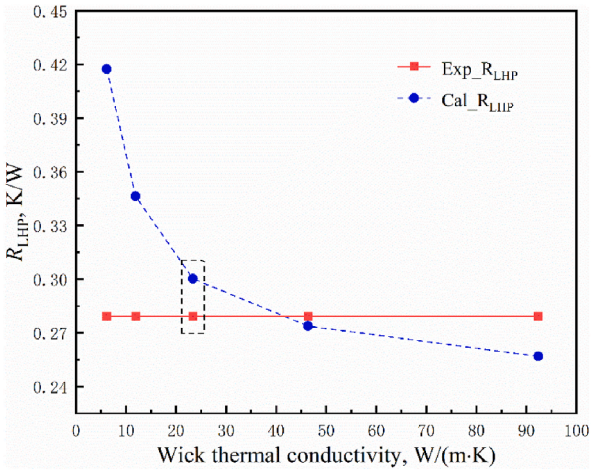

Fig. 13. The LHP thermal resistance with different wick thermal conductivities.

3.2. Comparison at various heat sink temperatures

Fig. 4 presents the comparison of numerical and experimental results on heating surface temperature and LHP thermal resistance while changing the heat sink temperature. The numerical results demonstrated that even if the heat sink temperature changed, the variation trends of heating surface temperature and LHP thermal resistance were still the same as those of experimental results. In addition to the extreme working conditions mentioned before, the maximum errors of heating surface temperature and thermal resistance were lower than 3.5 % and 17.7 % at heat sink temperature of 10 °C, 10.1 % and 15.1 % at heat sink temperature of −10 °C, respectively. Besides, the errors of heating surface temperature and thermal resistance were always kept below 5 % and 10 % in most heat load ranges. The errors of these numerical results were all within the acceptable range. Therefore, the numerical model was suitable for a variety of working conditions and could provide exact and instructive simulation results for subsequent parametric analysis study.

Another advantage of the numerical model was that the vapor volume percent distribution of LHP, which was unable to be estimated from experimental results, could be easily determined statistically from numerical results. As shown in Fig. 5, with the increase of heat load, the vapor volume in wick rose rapidly at first and then decreased gradually. The reason for this variation trend was that as the heat load ranged between 10 W and 40 W, the working fluid circulated too slowly owing to the low capillary force produced by wick. Heat load from heating surface was conducted deeply into the wick and the generated vapor could not discharge quickly, resulting in excessive vapor retention in wick. Once the heat load exceeded 40 W, a sufficient capillary force was generated in wick and the subcooled liquid accelerated back to the evaporator, quickly taking away the heat flux and vapor in wick, and thus reducing the vapor volume in wick. On top of that, the vapor volume in condenser kept growing due to the augmenter in circulation speed and vapor generation rate, and gradually stabilized under high heat load condition as the capillary force and condenser efficiency reached their maximum values. As the heat load reached the maximum, the vapor volume percent of wick was at a low value and the vapor volume percent of condenser even reduced, which also confirmed that the model was unable to calculate the dry-out state of wick. In addition to an apparent uptick observed at low heat load condition, the vapor volume percent of vapor collector remained generally greater than 80 %. Affected by the aforementioned variation trends in together, the total vapor volume of LHP varied between 15.2 % and 34.5 %, and the growth rate in the earlier period was larger than that in the later period. Changing the heat sink temperature also altered the variation trends of vapor volume percent at different fluid domains. Specifically speaking, lower heat sink temperature intensified the condenser cooling capacity, more vapor would gather inside and be quickly condensed into liquid. Consequently, as the heat sink temperature reduced, the upward trend of condenser vapor volume paced up at medium heat load condition, but the maximum value of condenser vapor volume was lower at high heat load condition.

4. Simulation results and discussions

4.1. Flow regime and vapor-liquid distribution analysis

Fig. 6 presents the temperature, stream line, and vapor-liquid interface distributions of vapor channel and evaporator central sections under the working condition of a heat sink temperature of 0 °C and a heat load of 80 W. As shown by the direction of fluid velocity vector, the stream line distribution of compensation chamber zone in Fig. 6 (a) indicated that the combined effect of inertial and gravity force induced the subcooled liquid to flow to the evaporator right side and scour the wick surface and compensation chamber wall nearby. Then the confinement of compensation chamber wall forced the liquid to flow back, forming a vortex above the wick surface. These fluid flow sequences led to an uneven distribution of subcooled liquid penetrating into the wick, which further resulted in a corresponding change of vapor-liquid interface. As shown in Fig. 6 (b), the vapor-liquid interface in wick appeared that the left side was deeper into the wick on account of less subcooled liquid supply. The action of capillary force kept the fluid in a downward direction, and by absorbing the heat load in wick, the liquid turned into vapor at the evaporation interface and flowed to

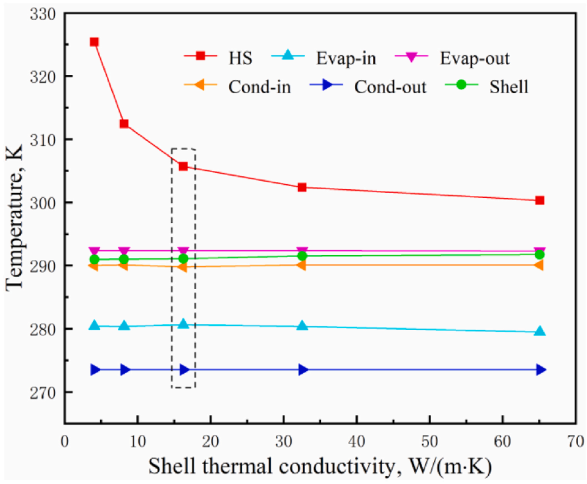

(a)

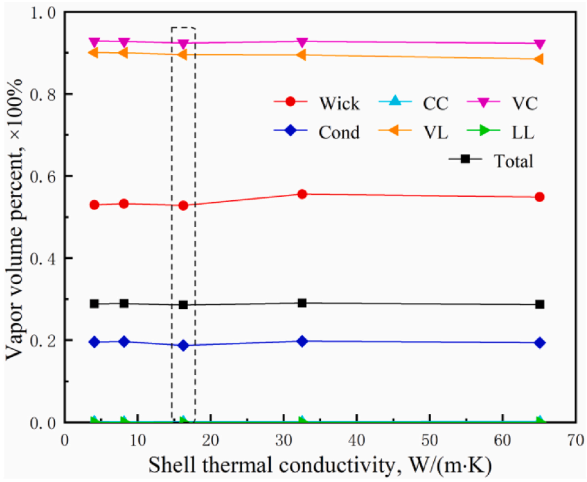

(b)

Fig. 14. Effect of different shell thermal conductivities on LHP components. (a) Temperature trend. (b) Vapor volume percent trend.

the vapor collector along the vapor channels. Fig. 6 (c) and (d) were the evaporator central sections in Y-direction. Confined by the compensation chamber walls, the fluid skimmed the wick surface on both sides, flowed back to the center, and merged with the main flow, forming two symmetric vortexes inside the compensation chamber. Attributing to the rib structure, heat conduct paths were created and the vapor-liquid interface at the rib root slightly penetrated into the wick than that at the vapor channels. Besides, the heat conduction by evaporator shell caused the vapor-liquid interface near the evaporator shell to penetrate deeper into the wick and even closer to the compensation chamber.

The uneven distribution of subcooled liquid in wick also affected the temperature distribution at different evaporator sections in Z-directions in Fig. 7. While the fluid first entered the evaporator from the inlet and scoured the wick surface and compensation chamber wall on the right side, a small amount of heat flux was absorbed, and the subcooled liquid became warmer as it returned to the evaporator left side. Hence, as shown in Fig. 7 (c), the wick surface in compensation chamber exhibited a trend that the temperature value on the left side was higher than the right side. Furthermore, this inhomogeneity of fluid subcooling degree distribution even caused the temperature on left side to be slightly higher than other places on both the heating surface and rib contact surface in Fig. 7(a) and (b). Contributing to the well heat conduction by the rib structure mentioned above, the temperature of contact area between two solid domain of rib structure and heating surface experienced a much lower degree. Conversely, the thick superheated vapor inside vapor channels hindered the heat transfer from heating surface to vapor-liquid interface where the heat load was mainly adsorbed. Thus the temperature on vapor channel surface was much higher than elsewhere.

4.2. Effect of wick porosity

Fig. 8 (a) and (b) present the temperature and vapor volume percent trends against various wick porosities at the constant working condition. The heat load was 80 W and the heat sink temperature was 0 °C. The middle group with black dashed box marked

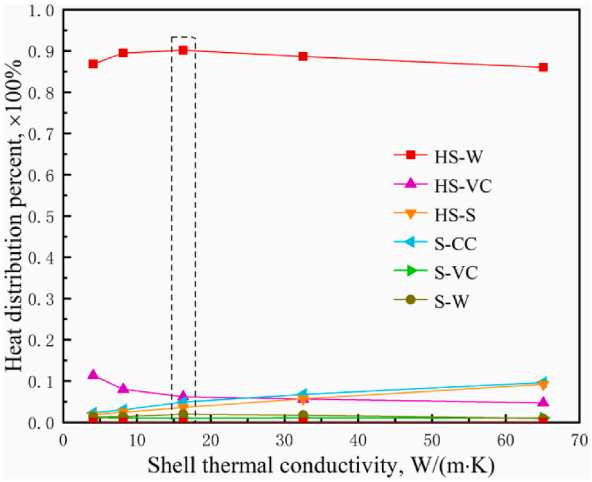

Fig. 15. Heat distribution of evaporator with different shell thermal conductivities.

was the control group with the same wick porosity condition as the experiment. The effect of porosity on capillary force was ignored for simplification, which meant that the momentum source term remained unchanged compared to the control group. When the wick porosity rose from 55 % to 95 % with an interval of 10 %, the permeability was enhanced and the penetration speed of subcooled liquid into the wick was enlarged. In addition, higher porosity brought about a sparser structure of the wick solid matrix, narrowing the heat conduct paths and reducing the wick effective thermal conductivity. Heat load from heating surface became more difficult to transfer to the vapor-liquid interface. Consequently, even the vapor volume percent of wick declined as more subcooled liquid entered, the heating surface temperature rose on the contrary. Once the porosity was up to 95 %, too much subcooled liquid flooded into the wick and caused a small amount of liquid to enter the vapor channel and collector. Thus, the temperature and vapor volume percent of fluid in the evaporator outlet and vapor collector dropped slightly, followed by these of fluid in the vapor line and condenser inlet. Since the wick was more vulnerable to being penetrated through by the vapor under the large porosity condition, a small number of bubbles even started to show up inside the compensation chamber. Moreover, the working fluid circulation was accelerated on such occasion, causing the temperatures of evaporator inlet and shell to drop by about 5 °C. Overall, the effect of porosity on condenser working performance was minimal for the vapor volume percent and temperature in the condenser remained nearly unchanged.

Fig. 9 presents the heat transfer percent between each component of evaporator at different wick porosities. Obviously, the heat transfer between heating surface and wick in the control group took away 90 % of the total heat load by the working fluid evaporation. The rest was mainly conducted to the shell and vapor channels, and was further absorbed by the subcooled liquid entering the compensation chamber and superheated vapor passing through the vapor channels. Higher porosity significantly narrowed the effective heat conduct path between heating surface and wick, which in turn caused more heat to be carried away by the high-speed vapor in the vapor channels. Numerically, the heat transfer percent between vapor channels and heating surface rose from 5 % to 20.4 % as the porosity rose from 55 % to 95 %, and the heat transfer between wick and heating surface shrank to 73 % at the maximum porosity. Likewise, a slight increment of heat transfer percent between heating surface and evaporator shell could be observed due to a corresponding increase in heat conduction to the evaporator shell.

Fig. 10 presents the system thermal performance, reflected by the LHP thermal resistance, against various wick porosities at the same working condition. As mentioned above, higher porosity resulted in less heat conduction to the vapor-liquid interface and weaker evaporation intensity accordingly, but more heat being taken away by the convection of fast-flowing vapor in channels. However, comparing with the high latent heat during evaporation, the low sensible heat of vapor could not quickly absorb the excess heat conducted to the vapor channels. A thicker and hotter superheated vapor gathered inside and deteriorated the evaporator working performance. Therefore, the LHP thermal resistance rose even faster over the entire range of wick porosity.

4.3. Effect of wick thermal conductivity

Fig. 11 (a) and (b) present the effect of wick thermal conductivity on temperature and vapor volume percent trends under the same working condition as before. Based on the porosity, liquid and solid matrix thermal conductivities, the wick thermal conductivity was calculated by the weight-averaged method,

$$k_{eff} = \phi k_l + (1 - \phi)\, k_{wick} \tag{48}$$

The solid matrix material of control group was nickel by reason of the sintered wick made of nickel powder in the experimental investigation. Since the study of wick porosity had been introduced above, the effect of wick thermal conductivity k_{eff} in this section was analyzed by escalating the solid matrix thermal conductivity k_{wick} from 22.94 W/(m·K) to 366.96 W/(m·K). The wick with high thermal conductivity reduced the difficulty of heat conduction from heating surface to vapor-liquid interface and elevated the evapora-

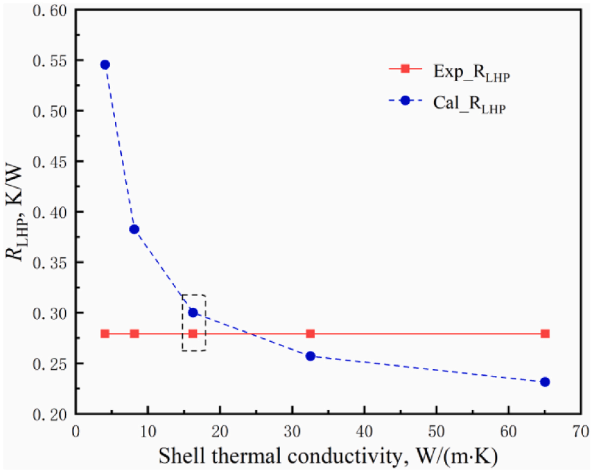

Fig. 16. The LHP thermal resistance with different shell thermal conductivities.

tion intensity in wick accordingly. The heat accumulated in heating surface was curtailed, and followed by the temperature reduction. Ascribing to the contact surface at the edge of wick, a small amount of heat was conducted from wick to evaporator shell as well, which answered for a small uptick in evaporator shell temperature. However, as shown in Fig. 11 (b), such abundant heat in wick inevitably raised the vapor volume percent inside, and even the vapor volume percent of compensation chamber started to increase due to the high rate of generated vapor penetrating through the wick. Except for having a significant impact on the working performance of evaporator, the wick thermal conductivity could not directly affect the thermo-hydraulic process of condenser, and two transport lines. As a result, the temperature and vapor volume percent of these places barely changed regardless of the variation of wick thermal conductivity.

Figs. 12 and 13 present the heat transfer percent between each component of evaporator and the LHP thermal resistance against various wick thermal conductivities. It could be seen clearly that a lower wick thermal conductivity resulted in additional heat that could not be conducted to wick being transferred to the evaporator shell and vapor channels, and the maximum of these two parts accounted for 6.5 % and 12.3 % of the total heat load, respectively. When the wick thermal conductivity enlarged from the minimum value, the heat conduction to the wick through ribs reinforced apparently in the early stage. But once the heat transfer between heating surface and wick exceeded 90 % of the total heat load, the improvement that could be produced by raising the wick thermal conductivity gradually became limited. Consequently, the growth rate of heat transfer percent between heating surface and wick slowed down in the later stage. Besides, the more heat that was conducted to wick, the stronger the evaporation intensity of fluid on vapor-liquid interface, the better the evaporator working performance. Hence, the LHP thermal resistance showed the opposite trend to the heat transfer percent between heating surface and wick, and in the early stage, the decline was faster than that in the later stage. Generally speaking, the LHP thermal resistance could be diminished by up to 38.5 % via enlarging the wick thermal conductivity in simulation.

4.4. Effect of shell thermal conductivity

As with the wick thermal conductivity, the shell thermal conductivity also had a certain effect on the evaporator thermal performance. During the previous experimental investigation, the heating surface and evaporator shell were both made from SS304. For this reason, the thermal conductivity of heating surface was always set to be the same as that of the shell in the numerical simulation. As indicated in Fig. 14 (a), higher thermal conductivity avoided heat accumulation in heating surface and enhanced the heat conduction through evaporator shell. However, Due to the large contact surface between heating surface and wick, the heat transfer percent from heating surface to shell was much lower than that to wick. Meanwhile, the subcooled liquid in the compensation chamber quickly absorbed the heat from the shell. Consequently, the evaporator shell temperature experienced only a slight increase compared to the significant reduction in heating surface temperature. Furthermore, when the shell thermal conductivity was big enough, the heat transfer speed of heating surface to wick came to its limit, resulting in a slowdown in the descent rate of heating surface temperature. Despite the apparent temperature change being induced, the effect of shell thermal conductivity on the distribution of vapor volume percent was small. Only a 2 % increment was observed in vapor volume percent of wick in Fig. 14 (b). This accounted for a minimal correlation between the heat conduction of shell and the evaporation process of the fluid in wick.

Fig. 15 presents the variation trends of heat transfer percent between different components of evaporator. While the shell thermal conductivity was below the control group, the intensity of heat conduction from heating surface to wick and shell was brought down. The fast flow of superheated vapor took away more heat in vapor channels instead, and the corresponding heat transfer percent rose to 11.3 % of the total heat load. Moreover, the thick vapor layer on this occasion offered a smaller vapor-liquid interface than the porous structure in wick, which further worsened the proper working condition of evaporator. As shown in Fig. 16, the LHP thermal resistance highly proliferated compared with the control group. When the shell thermal conductivity enlarged, the heat transfer between heating surface and wick, heating surface and shell, shell and compensation chamber were directly intensified. Heat absorbed

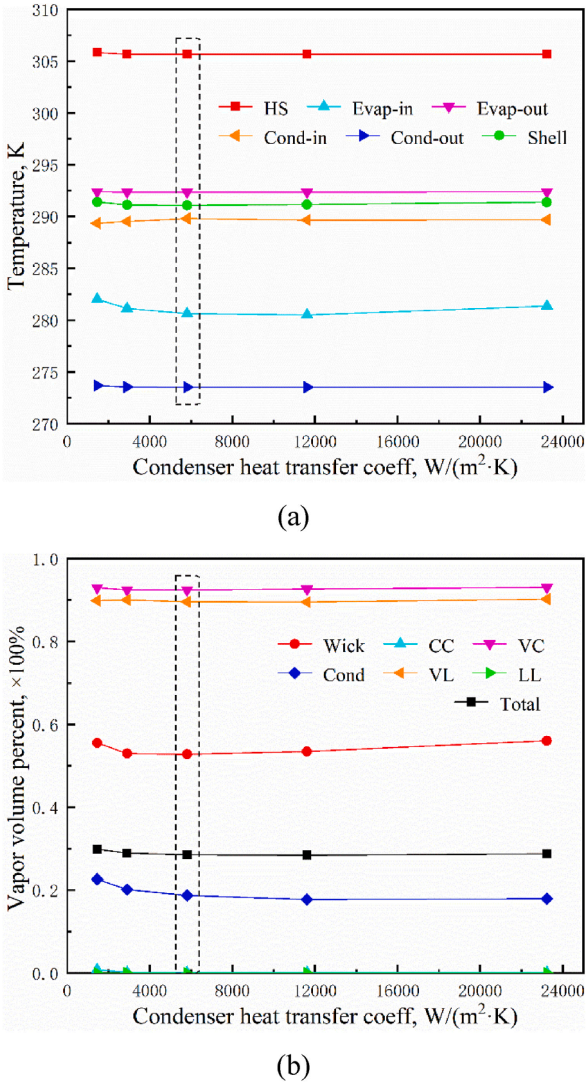

Fig. 17. Effect of different condenser heat transfer coefficients on LHP components. (a) Temperature trend. (b) Vapor volume percent trend.

by the evaporation was greater and the LHP thermal resistance performed the same variation pattern as in Fig. 13. The residual heat left to the superheated vapor in vapor channels declined and the heat transfer percent between vapor channels and heating surface shrank. However, once the shell thermal conductivity was higher than that of the wick in control group and continued to increase, the sufficient subcooled liquid in compensation chamber adsorbed heat more easily by the fluid sensible heat and this heat transfer enhancement was even larger than that of the evaporation. Thus, a slight decrease in heat transfer percent between heating surface and wick could be observed under the situation of elevation in heat transfer percent between heating surface and shell, shell and compensation chamber.

4.5. Effect of condenser heat transfer coefficient

Fig. 17 (a) and (b) present the temperature and vapor volume percent trends of LHP system against various condenser heat transfer coefficients. Apparently, the lower the condenser heat transfer coefficient, the more noticeable the influence on the LHP working performance. The condensation efficiency depended on the condenser heat transfer coefficient. As the condensation efficiency reduced, the vapor became more difficult to cool into a subcooled liquid state before leaving the condenser and the vapor volume percent of wick enlarged consequently. On account of the fixed value of driving force set in the model, the growth of two-phase section length in condenser raised the flow resistance inside, thereafter slowing down the circulation of working fluid. In addition, the heat leak from heating surface to evaporator shell slightly increased the temperatures at shell and evaporator inlet. Therefore, as the subcooled liquid that penetrated the wick turned into a warmer fluid, the vapor volume percent of wick elevated. Aside from the above variation, the temperature and vapor volume percent of other places were barely changed. When the condenser heat transfer coeffi-

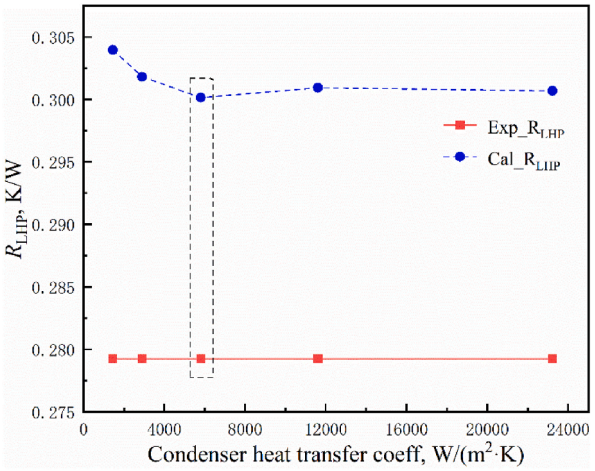

Fig. 18. The LHP thermal resistance with different condenser heat transfer coefficients.

cient was high enough, the cooling speed of vapor reached its limit. The vapor volume percent of condenser gradually stabilized and no more improvement could be given to the LHP working performance.

Fig. 18 presents the LHP thermal resistance against condenser heat transfer coefficient. For the working condition of low condenser heat transfer coefficient, the insufficient subcooling degree of working fluid entering the wick cut down the evaporator working capacity. In the case of simultaneous degradation of evaporator and condenser performance, the system operating performance deteriorated and an up-regulation could be found in the LHP thermal resistance. Hence, it demonstrated an opposite trend compared with the condenser heat transfer coefficient. Meanwhile, once the condenser heat transfer coefficient was greater than that of the control group, the condensation efficiency reached its maximum and the LHP thermal resistance no longer decreased.

5. Conclusions

In this paper, an effective 3-D CFD numerical model was proposed for determining the thermo-hydraulic behavior of two-phase flow in a square evaporator LHP at the system scale. The VOF method was adopted as the multiphase flow model and the system driving force was determined through the flow resistance analysis combined with experimental results. In addition, parametric analysis was carried out by studying the effects of different parameters, including heat sink temperatures, porosities, wick and shell thermal conductivities, and condenser heat transfer coefficients, on LHP thermal performance. The conclusions were as follows.

1. Experimental validation at various heat sink temperatures and heat loads indicated that the calculation results followed well with the test results. In addition to the maximum and minimum heat loads, the maximum error of heating surface at heat sink temperature of 0 °C was below 5.2 %, proving that the model had good precision and could provide instructive simulation results for the parametric analysis study.
2. The structural constraint and gravity effect led to an inhomogeneous but symmetrical distribution of subcooled liquid flow with two vortexes in the compensation chamber. Therefore, the vapor-liquid interface on the left side of wick was deeper and closer to the compensation chamber, and the heating surface temperature on left side was slightly higher than other areas.
3. A higher porosity narrowed the thermal path from heating surface to vapor-liquid interface in wick and ensured more subcooled liquid entering the wick. The vapor volume percent of wick declined and the heating surface temperature elevated conversely. Besides, the heat transfer percent between heating surface and wick decreased, making it more challenging to take away heat by relying solely on the sensible heat of superheated vapor, and resulting in increased LHP thermal resistance.
4. Raising the wick and shell thermal conductivities both brought down the heating surface temperature by facilitating the heat conduction effect. More heat would be transferred from heating surface into wick at a certain extent. The evaporation intensity was enhanced and the LHP thermal resistance sustained a downward trend accordingly. When the shell thermal conductivity was large enough, the heat conduction from heating surface to shell was more intense and the heat transfer from heating surface to wick even suffered a slight reduction.
5. The condenser cooling capacity deteriorated as the heat sink temperature augmented, and followed by a slower upward trend of vapor volume percent of condenser but a higher value at high heat load condition. Enlarging the condenser heat transfer coefficient improved the evaporator working capacity indirectly by lowering down the vapor volume percent of condenser and wick. In the case of high condenser heat transfer coefficient, the downward trend of LHP thermal resistance slowed down and stabilized eventually as the condensation efficiency reached its limit.

CRediT authorship contribution statement

Zikang Zhang: Writing – review & editing, Writing – original draft, Visualization, Validation, Software, Methodology, Investigation, Formal analysis, Data curation, Conceptualization. **Haichuan Cui:** Software, Formal analysis. **Zhenyuan Ma:** Visualiza-

tion, Investigation. **Yifan Zhang:** Resources, Investigation. **Zhichun Liu:** Writing – review & editing, Supervision, Resources, Project administration, Funding acquisition, Conceptualization. **Wei Liu:** Writing – review & editing, Supervision, Resources, Project administration, Funding acquisition, Conceptualization.

Declaration of competing interest

To the best of our knowledge and belief, neither I nor any coauthors have any possible conflicts of interest.

Data availability

No data was used for the research described in the article.

Acknowledgements

This work was supported by the National Natural Science Foundation of China (No. 51736004 and No. 52076088).

Nomenclature

A_w	wick surface area [m^2]
coeff	mass transfer coefficient [s^{-1}]
C_1	viscous resistance factor [m^{-2}]
C_2	inertial resistance factor [m^{-1}]
d_b	bubble diameter [m]
d_p	average pore diameter inside the wick [m]
d_t	average hydraulic diameter [m]
E	specific energy [J kg^{-1}]
F_{vol}	source term of surface tension [kg m^{-2} s^{-2}]
g	gravity [N kg^{-1}]
h	sensible enthalpy [m^2 s^{-2}]
h_{fg}	latent heat of working fluid [J kg^{-1}]
h_z	local heat transfer coefficient [W m^{-2} K^{-1}]
k	thermal conductivity [W m^{-1} K^{-1}]
K	wick permeability [m^2]
l	flow line length [m]
L_w	capillary structure thickness [m]
m_f	mass flow rate of fluid [kg/s]
M	relative molecule mass [1]
p	pressure [Pa]
P	pressure loss [Pa]
Q	heat load at heating surface [W]
R	thermal resistance [°C W^{-1}]
R_g	universal gas constant [J mol^{-1} K^{-1}]
S_{cap}	capillary force source term [pa m^{-1}]
$S_{m,l}$	liquid source term [kg m^{-3} s^{-1}]
$S_{M,i}$	i-th phase momentum source term [pa]
$S_{m,v}$	vapor source term [kg m^{-3} s^{-1}]
S_q	heat source term [W m^{-3}]
t	time [s]
T	temperature [K]
u	velocity [m s^{-1}]
$\boldsymbol{u}$	velocity vector [m s^{-1}]
Greek symbol	
α	volume fraction
ε	error [%]
ζ	local resistance coefficient
θ	liquid contact angle [°]
κ	interphase curvature [m-1]
μ	dynamic viscosity [N s m-2]
ξ	friction factor of fluid
π	Pi
ρ	density [kg m-3]
σ	surface tension coefficient [N m-1]
ϕ	wick porosity [%]
Subscripts	
a	acceleratory pressure drop

(*continued on next page*)

(*continued*)

cal	calculation
cap	capillary force
cap,max	maximum capillary force
cc	compensation chamber
cond	condenser
eff	effective value
evap	evaporator
evap_in	evaporator inlet
exp	experiment
f	frictional pressure drop
g	gravity/gravitational pressure drop
l	liquid
LHP	loop heat pipe
ll	liquid line
loc	local pressure loss
s	solid material
sat	saturation
tot	total
v	vapor
vch	vapor channels
vco	vapor collector
vis	viscous pressure loss
vl	vapor line
w	wick
x	dryness degree of the fluid
Abbreviations	
Cal	calculation results
CC	vapor volume percent of compensation chamber
Cond	vapor volume percent of condenser
Cond-in	condenser inlet
Cond-out	condenser outlet
Exp	experiemtal results
Evap-in	evaporator inlet
Evap-out	evaporator outlet
HS	heating surface
LHP	loop heat pipe
LL	vapor volume percent of liquid line
Nu	the Nusselt number
Pr	the Prandtl number
R	thermal resistance
Re	the Reynolds number
S	evaporator shell
Shell	evaporator shell
SS304	stainless steel 304
Total	vapor volume percent of the whole LHP system
VC	vapor volume percent of vapor collector
VL	vapor volume percent of vapor line
Wick	vapor volume percent of wick

References

[1] Y.F. Maydanik, Loop heat pipes, Appl. Therm. Eng. 25 (2005) 635–657 %@ 1359-4311.
[2] J.I. Rodriguez, A. Na-Nakornpanom, J.G. Rivera, V. Mireles, H. Tseng, On-orbit performance of the TES loop heat pipe heat rejection system, in: SAE Technical Paper, 2008.
[3] T. Gao, T. Yang, S.L. Zhao, Q.L. Meng, The design and application of temperature control loop heat pipe for space CCD camera, in: International Symposium of Space Optical Instrument and Application, Springer, 2017, pp. 65–74.
[4] T. Shioga, Y. Mizuno, H. Nagano, Operating characteristics of a new ultra-thin loop heat pipe, Int. J. Heat Mass Tran. 151 (2020) 119436.
[5] M. Mochizuki, Y. Saito, T. Nguyen, T. Nguyen, V. Wuttijumnong, Y. Horiuchi, R. Tacomkang, R. Singh, A. Akbarzadeh, Development of miniature loop heat pipes for the thermal control of laptops, International Conference on Micro/Nanoscale Heat Transfer 42924 (2008) 969–974.
[6] J. Li, G.H. Zhou, T. Tian, X.P. Li, A new cooling strategy for edge computing servers using compact looped heat pipe, Appl. Therm. Eng. 187 (2021) 116599.
[7] M.A. Chernysheva, S.I. Yushakova, Y.F. Maydanik, Copper-water loop heat pipes for energy-efficient cooling systems of supercomputers, Energy 69 (2014) 534–542.
[8] R. Singh, T. Nguyen, Loop heat pipes for thermal management of electric vehicles, J. Therm. Sci. Eng. Appl. 14 (2021) 061010.
[9] B. Ariantara, N. Putra, S. Supriadi, Battery thermal management system using loop heat pipe with LTP copper capillary wick, in: IOP Conference Series: Earth and Environmental Science, 105, IOP Publishing, 2018 012045.
[10] N. Watanabe, T. Mizutani, H. Nagano, High-performance energy-saving miniature loop heat pipe for cooling compact power semiconductors, Energy Convers. Manag. 236 (2021) 114081.
[11] Y.F. Maydanik, S.V. Vershinin, M.A. Chernysheva, The results of comparative analysis and tests of ammonia loop heat pipes with cylindrical and flat evaporators, Appl. Therm. Eng. 144 (2018) 479–487.
[12] X.Q. Li, D.X. Yao, K.H. Zuo, Y.F. Xia, Y.P. Zeng, Effects of pore structures on the capillary and thermal performance of porous silicon nitride as novel loop heat pipe wicks, Int. J. Heat Mass Tran. 169 (2021) 120985.

[13] A. Amhar, N. Putra, Development and testing multiple evaporator loop heat pipe utilizing three way T port valve, in: AIP Conference Proceedings, 2255, AIP Publishing, 2020.
[14] S. Ahmed, C. Nashine, M. Pandey, Thermal management at microscale level: detailed study on the development of a micro loop heat pipe, Micro and Nano Engineering 16 (2022) 100150.
[15] T. Tharayil, L.G. Asirvatham, V. Ravindran, S. Wongwises, Thermal performance of miniature loop heat pipe with graphene-water nanofluid, Int. J. Heat Mass Tran. 93 (2016) 957–968.
[16] L. Liu, B. Yuan, C.Y. Cui, X.P. Yang, J.J. Wei, Investigation of a loop heat pipe to achieve high heat flux by incorporating flow boiling, Int. J. Heat Mass Tran. 195 (2022) 123173.
[17] I. Setyawan, N. Putra, I.I. Hakim, Experimental investigation of the operating characteristics of a hybrid loop heat pipe using pump assistance, Appl. Therm. Eng. 130 (2018) 10–16.
[18] B. Siedel, V. Sartre, F. Lefevre, Complete analytical model of a loop heat pipe with a flat evaporator, Int. J. Therm. Sci. 89 (2015) 372–386.
[19] A.E. Belov, A.A. Velikanov, D.N. Il'mov, O.A. Nagornova, V.V. Sobolev, N.I. Filatov, Numerical and experimental study of loop heat pipe steady-state performance, Therm. Eng. 69 (2022) 190–201.
[20] L.Z. Bai, J.H. Guo, G.P. Lin, J. He, D.S. Wen, Steady-state modeling and analysis of a loop heat pipe under gravity-assisted operation, Appl. Therm. Eng. 83 (2015) 88–97.
[21] T. Tharayil, L.G. Asirvatham, M.J. Dau, S. Wongwises, Entropy generation analysis of a miniature loop heat pipe with graphene-water nanofluid: thermodynamics model and experimental study, Int. J. Heat Mass Tran. 106 (2017) 407–421.
[22] Z.G. Qu, G. Chen, L. Zhou, J.Y. Miao, Numerical study on the operating characteristics of cryogenic loop heat pipes based on a one-dimensional heat leak model, Energy Convers. Manag. 172 (2018) 485–496.
[23] S. Meinicke, P. Knipper, C. Helfenritter, T. Wetzel, A lean approach of modeling the transient thermal characteristics of loop heat pipes based on experimental investigations, Appl. Therm. Eng. 147 (2019) 895–907.
[24] X.X. Liu, H.W. Liu, X.D. Zhao, Z.H. Han, Y. Cui, M. Yu, A novel neural network and grey correlation analysis method for computation of the heat transfer limit of a loop heat pipe (LHP), Energy 259 (2022) 124830.
[25] M. Bernagozzi, S. Charmer, A. Georgoulas, I. Malavasi, N. Miché, M. Marengo, Lumped parameter network simulation of a Loop Heat Pipe for energy management systems in full electric vehicles, Appl. Therm. Eng. 141 (2018) 617–629.
[26] J. Li, G.P. Peterson, 3D heat transfer analysis in a loop heat pipe evaporator with a fully saturated wick, Int. J. Heat Mass Tran. 54 (2011) 564–574.
[27] K. Fukushima, H. Nagano, New evaporator structure for micro loop heat pipes, Int. J. Heat Mass Tran. 106 (2017) 1327–1334.
[28] M.A. Chernysheva, V.G. Pastukhov, Y.F. Maydanik, Analysis of heat exchange in the compensation chamber of a loop heat pipe, Energy 55 (2013) 253–262.
[29] X.F. Zhang, X.Y. Li, S.F. Wang, Three-dimensional simulation on heat transfer in the flat evaporator of miniature loop heat pipe, Int. J. Therm. Sci. 54 (2012) 188–198.
[30] J. Li, F.J. Hong, R.J. Xie, P. Cheng, Pore scale simulation of evaporation in a porous wick of a loop heat pipe flat evaporator using Lattice Boltzmann method, Int. Commun. Heat Mass Tran. 102 (2019) 22–33.
[31] L. Mottet, M. Prat, Numerical simulation of heat and mass transfer in bidispersed capillary structures: application to the evaporator of a loop heat pipe, Appl. Therm. Eng. 102 (2016) 770–784.
[32] Y.X. Zhang, J.Y. Liu, L.F. Liu, H.L. Jiang, T. Luan, Numerical simulation and analysis of heat leakage reduction in loop heat pipe with carbon fiber capillary wick, Int. J. Therm. Sci. 146 (2019) 106100.
[33] A.A. Pozhilov, D.K. Zaitsev, E.M. Smirnov, A.A. Smirnovsky, Numerical simulation of heat and mass transfer in a 3D model of a loop heat pipe evaporator, St. Petersburg Polytechnical University Journal: Physics and Mathematics 3 (2017) 210–217.
[34] W.H. Lee, A pressure iteration scheme for two-phase flow modeling, Multiphase transport fundamentals, reactor safety, applications 1 (1980) 407–431.
[35] J.D. Anderson, J. Wendt, Computational Fluid Dynamics, McGraw-Hill, New York, 1995.
[36] H. Hertz, On the evaporation of liquids, especially mercury, in vacuo, Ann. Phys. 17 (1882) 178–193.
[37] M. Knudsen, Maximum rate of vaporization of mercury, Ann. Phys. 47 (1915) 697–705.
[38] A. Fluent, ANSYS Fluent Theory Guide, ANSYS Inc., Canonsburg, PA, USA, 2019.
[39] P. Datta, A. Chakravarty, K. Ghosh, A. Mukhopadhyay, S. Sen, Modeling of steam-water direct contact condensation using volume of fluid approach, Numer. Heat Tran., Part A: Applications 73 (2018) 17–33.
[40] J.U. Brackbill, D.B. Kothe, C. Zemach, A continuum method for modeling surface tension, J. Comput. Phys. 100 (1992) 335–354.
[41] S. Ergun, Fluid flow through packed columns, Chem. Eng. Prog. 48 (1952) 89–94.
[42] Z.K. Zhang, H.C. Cui, S.C. Zhao, R.Z. Zhao, T. Wu, Z.C. Liu, W. Liu, Simulation of heat and mass transfer process in a flat-plate loop heat pipe and experimental comparison, Appl. Therm. Eng. (2022) 119705.
[43] M. Kaviany, Principles of Heat Transfer in Porous Media, Springer Science & Business Media, 2012.
[44] J. Weisbach, Lehrbuch der ingenieur-und maschinen-mechanik, F. Vieweg und Sohn, 1850.
[45] W.R. Lockhart, R.C. Martinelli, Proposed correlation of data for isothermal two-phase, two-component flow in pipes, Chem. Eng. Prog. 45 (1949) 39–48.
[46] D.P. Traviss, A.G. Baron, W.M. Rohsenow, Forced-convection condensation inside tubes: a heat transfer equation for condenser design, Build. Eng. 79 (1973) 157–165.